Propulsion performance of a two-dimensional flapping airfoil with wake map and dynamic mode decomposition analysis

Hongyu Zheng, Fangfang Xie* Yao Zheng, Tingwei Ji, and Zaoxu Zhu
Center for Engineering and Scientific Computation, and School of Aeronautics and Astronautics Zhejiang University, Zhejiang 310027, China

(Received 21 January 2019; revised manuscript received 29 May 2019; published 26 June 2019)

In the present study, we use the dynamic mesh method based on the radial basis function interpolation for the two-dimensional simulation of harmonically oscillating NACA0015 airfoil. Under various flapping frequencies, heaving and pitching amplitudes, the observed wake flows can be divided into seven types, including the Bénard-von Kármán (BvK) vortex street, the reversed BvK (RBvK) vortex street, the $1P$ wake, the mP wake, the $2P + mS$ wake, the $2S + mS$ wake, and the mS wake, where m is around 4 and $xS + yP$ signifies x single vortices and y vortex pairs shedding per oscillation period. Then we have constructed two phase diagrams of the wake types in terms of the flapping frequency, heaving and pitching amplitudes. Importantly, we have combined the propulsion performance of the flapping airfoil with the wake map and found that $\alpha(\frac{T}{4})$, the angle of attack at $t = T/4$, can determine the wake type: negative value corresponding to drag-dominated wakes, while positive value corresponding to thrust dominated flow wakes. With the increase of $\alpha(\frac{T}{4})$, the wake transforms from the mP to $2S + mS$ then to RBvK and eventually to $1P$ wake. Furthermore, the coherent structure analysis and spectral analysis are conducted for all the types of wakes by using dynamic mode decomposition. And there is a positive correlation between the strengths of vortices shedding at i times flapping frequency and the modulus of the ith dynamic mode decomposition mode, which can further reveal the differences among different types of wakes.

DOI: 10.1103/PhysRevE.99.063109

I. INTRODUCTION

After billions of years of evolution, birds, as well as fish and insects, have developed a highly efficient movement, and their elegant structure and nimble flapping are capable of producing high lift, thrust, and propulsion efficiency [1]. The mysterious aerodynamics mechanisms behind flapping wings have drawn extensive attention for a long time due to their potential to enable the development of flapping wing microair vehicles.

The extensive studies have been conducted on exploring the basic aspects of the wake formation and the associated fluid forces of flapping airfoil [2–6], particularly on the drag-thrust transition and its relation to the changes in wake structures [7–9]. Young *et al.* [10] presented that the Strouhal number ($\mathrm{St} = fA/U_\infty$) can determine the categories of the wake flows of plunging airfoil as drag-producing, neutral and thrust-producing. The drag-producing wake resembles the Bénard-von Kármán (BvK) vortex street while the thrust-producing wake emerges the reversed BvK (RBvK) vortex street. Godoy-Diana *et al.* [11] experimentally identified the transition from the BvK wake to RBvK vortex street in the flapping frequency-amplitude phase space and showed that the wake transition precedes the actual drag-thrust transition for the plunging airfoil. Furthermore, by using the number of the single vortices and vortex pairs to label the wake, Schnipper *et al.* [12] and Andersen *et al.* [13] mapped out a phase diagram to investigate the drag-thrust transition. In these studies, the airfoil only oscillates with two simplified kinematic modes: pure heaving and pure pitching.

For the flapping airfoil combining heaving and pitching motions, Triantfyllou *et al.* [14,15] studied the effects of the Strouhal number and the maximum angle of attack (AOA) on the thrust force and on the hydro-mechanical efficiency. Kinsey *et al.* [16] further presented a mapping of power-extraction efficiency in the frequency and pitching-amplitude space and confirmed the importance of the AOA and leading-edge vortices (LEVs) in the high propulsion efficiency. However, the correlation between the wake types and the drag-thrust transitions needs further analysis. In the current study, we will construct two phase diagrams of the flow wakes in terms of the flapping frequency, heaving and pitching amplitudes. In the meanwhile, we will combine the propulsion efficiency contour with the wake map and investigate the correlation between the wake structures and aerodynamic forces. The effects of the effective AOA on the wake structures will be emphatically discussed.

In the post processing, mode reduction method, such as dynamic mode decomposition (DMD) [17], has become a useful technique to analyze a complex flow field. DMD method can not only extract dominated coherent structures from the flow fields generated by either experiments or numerical simulations but also obtain the corresponding dynamic information [18,19]. Bagheri [17] decomposed the flow past a cylinder into a sequence of Koopman modes to analyze

*fangfang_xie@zju.edu.cn

the first Hopf bifurcation. Mohan *et al.* [20] applied DMD to the plunging airfoil to analyze the deep dynamic stall, and further investigated the correlation between the DMD modes and proper orthogonal decomposition (POD) modes. Pan *et al.* [21] obtained the vortex shedding pattern behind the trailing edge of Gurney flap, and its high-order harmonics had been captured with frequency, wavelength and convection speed. All these attempts give us new inspirations to explore the underlying physical mechanisms of the flapping airfoil by using DMD analysis in the current study. Moreover, we will apply the virtual force calculation [22] on the DMD modes to relate the coherent structures with the aerodynamic forces.

The outline of this paper is organized as follows: In Sec. II, the numerical methods, simulation setup, and validation are briefly described. In Sec. III, we will draw the wake maps of the flapping foil in various parameter space and reveal the relationship between the wake structures and the propulsion performance. In Sec. IV, the effect of the effective angle of attack is investigated. In Sec. V, we will show DMD analysis of the flow wakes. In Sec. VI, we draw the conclusions.

II. COMPUTATIONAL METHODOLOGY AND POST-PROCESSING TOOLS

A. The finite-volume method

In the current study, the open-source code OpenFOAM [23] is used for the simulation of the flapping airfoil. We assume the flow incompressible and apply the arbitrary Lagrangian-Eulerian [24] method to discretize Navier-Stokes equations on the moving grids. The arbitrary Lagrangian-Eulerian method combines the Lagrangian and Eulerian descriptions, which means that not only the mesh can deform with the boundary motion but also the fluid can flow through the mesh. For arbitrary control volume V the governing equation can be derived as follows:

$$\frac{d}{dt}\int_V \rho \mathbf{U} dV + \oint_S \mathbf{ds}\cdot\rho(\mathbf{U}-\mathbf{U}_s)\mathbf{U} = \oint_S \mathbf{ds}\cdot(-p\mathbf{I}+\rho\nu\nabla\mathbf{U}), \tag{1}$$

$$\frac{d}{dt}\int_V dV - \oint_S \mathbf{ds}\cdot\mathbf{U}_s = 0, \tag{2}$$

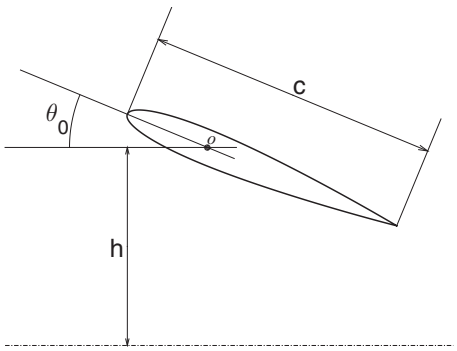

FIG. 1. The sketch of the flapping foil.

TABLE I. Group 1.

Kinetics parameters	
Frequency	0.06, 0.08, 0.10, 0.12, 0.14, 0.16, 0.18, 0.20, 0.225, 0.25, 0.275, 0.30
Heaving amplitude	1
Pitching amplitude	0.087, 0.175, 0.349, 0.524, 0.698, 0.873

where S is the boundary surface of the control volume, $\mathbf{U}_s$ is the velocity of the moving surface and $\mathbf{U}$ is the flow velocity, ρ is the density, p is the pressure, and ν is the kinetic viscosity.

In the current study, the space discretizations are second-order upwind for the convection terms and central differences for the Laplacian terms, respectively. For the time discretization, the second-order backward Euler scheme is adopted. Then the pressure and velocity equations are coupled by the PISO algorithm and two pressure correction loops are used. The pressure equations are solved by the preconditioned conjugate gradient (PCG) solver and the velocity equations are treated by the preconditioned biconjugate gradient (PBiCG) solver.

B. Dynamic mesh method

For the dynamic mesh, the radial basis function interpolation [25] is used, which can improve the accuracy and efficiency of dynamic meshes when the rotation of boundary around the flapping foil is high. Besides, unlike the classical spring analogy formulations, the dynamic mesh based on radial basis function interpolation leaves out the grid adjacency relationship. Specifically, given the boundary movements, the radial basis function interpolation holds that the displacements of internal points are only related with the Euclidean distances between the internal points and boundary points, which reduces the computational cost. A detailed explanation of the method can be found in Appendix A.

C. Simulation setup

The airfoil used in the current study is NACA0015. As shown in Fig. 1, the flapping airfoil can both heave and pitch. The kinematic equations are given by

$$y(t)/c = h\sin(2\pi ft+\phi), \tag{3}$$

$$\theta(t) = \theta_0\sin(2\pi ft), \tag{4}$$

where h is nondimensional heaving amplitude, θ_0 is pitching amplitude, and f is flapping frequency. The Reynolds number $\mathrm{Re} = Uc/\nu$ is set to 1100, where c is the length of the chord and U is the free-stream velocity. The initial phase difference between the heaving and pitching ϕ is set to $\pi/2$, the pivoting

TABLE II. Group 2.

Kinetics parameters	
Frequency	0.15
Heaving amplitude	0.050, 0.125, 0.250, 0.375, 0.500, 0.625, 0.750, 0.875, 1.000, 1.250
Pitching amplitude	0.087, 0.175, 0.349, 0.524, 0.698, 0.873

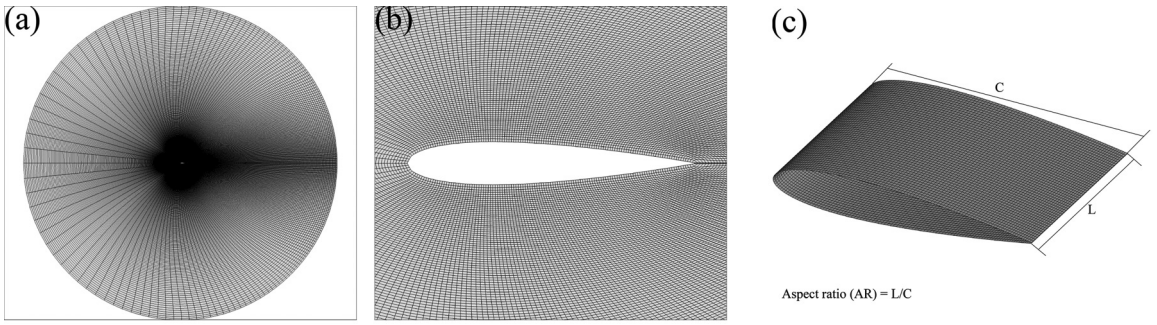

FIG. 2. The sketch of the two-dimensional and three-dimensional meshes: (a) the holistic view of the two-dimensional mesh; (b) the close view of the two-dimensional mesh; (c) the surface mesh of the airfoil in the three-dimensional mesh.

point o is located at the chord line of the airfoil with a distance of $0.3c$ from the leading edge.

Furthermore, we divide all the cases into two groups, as shown in Tables I and II. In group 1, the heaving amplitude is fixed while the frequency and the pitching amplitude are freely combined. In group 2, the frequency is fixed while the heaving and pitching amplitudes are freely combined.

In the present study, we will focus on the aerodynamic performance of the flapping airfoil by evaluating the thrust coefficient C_T, lift coefficient C_L, and propulsion efficiency η, which are defined as follows:

$$C_T = \frac{T}{\frac{1}{2}\rho U_\infty^2 c}, \tag{5}$$

$$C_L = \frac{L}{\frac{1}{2}\rho U_\infty^2 c}, \tag{6}$$

$$\eta = \frac{P_{\text{out}}}{P_{\text{in}}}, \tag{7}$$

with

$$P_{\text{in}} = \int_0^{t_{\text{cir}}} \left[-L(t)\frac{dy}{dt} - M(t)\frac{d\theta}{dt} \right] dt, \tag{8}$$

$$P_{\text{out}} = \int_0^{t_{\text{cir}}} T(t) U_\infty dt, \tag{9}$$

where t_{cir} is one or several periods, T is the thrust, L is the lift, and M is the torque at the pivot point.

D. Computational domain and solver validation

A circular computational domain with the radius of $30c$ is used in the current study. It is discretized with a structured O-type mesh, as can be seen in Fig. 2. In the two-dimensional (2D) x-o-y plane, 259 grid points lay on the airfoil surface and the height of the first layer is $0.01c$, where c is the chord length. For three-dimensional (3D) simulations, the 2D mesh is extruded to a 3D domain. For the outside boundary, the velocity condition is no-slip and the pressure is constant. For the airfoil, the moving wall and zero normal pressure gradient conditions are used. Then we initialize the flow with a constant velocity field.

For the validation, a 2D grid convergence with five mesh resolutions is firstly conducted. The kinematic parameters are set as $f = 0.25$, $h = 1$, $\theta_0 = 30^\circ$. As shown in Fig. 3, the mesh resolution is converged when the grid number is over 102 942. Then the effects of the simulation time step (dt) and the radius (R) of the computation domain on the thrust coefficient are shown in Fig. 4. It is indicated that the temporal resolution is converged when the time step reaches 0.001 s and the effect of the computation domain size is weak.

For the 3D simulations, a grid convergence with various spanwise domain sizes and spanwise mesh density is firstly studied. As shown in Fig. 5(a), the mesh resolution is converged when the spanwise mesh size reaches $0.02c$ for the aspect ratio of $AR = 1$. While by fixing the spanwise mesh size ($dz = 0.02c$), the effect of aspect ratio on the simulations is very week, as seen in Fig. 5(b). Therefore, the grid with

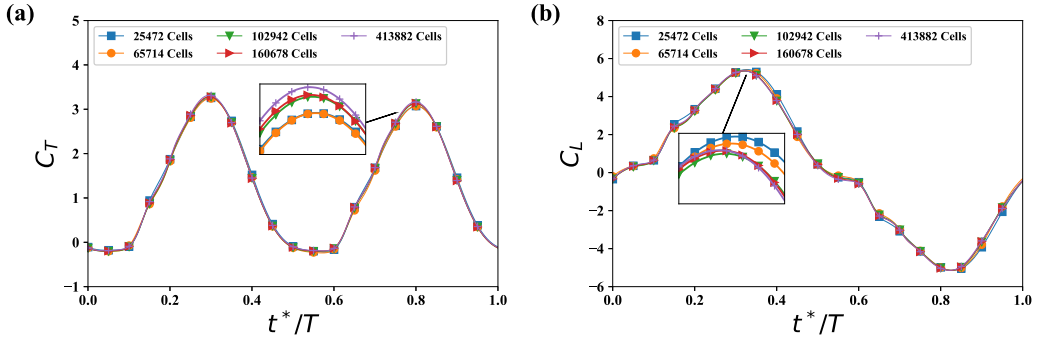

FIG. 3. The gird convergence results for the two-dimensional flapping airfoil with kinematic parameters ($f = 0.25$, $h = 1$, $\theta_0 = 30^\circ$): (a) thrust coefficient; (b) lift coefficient.

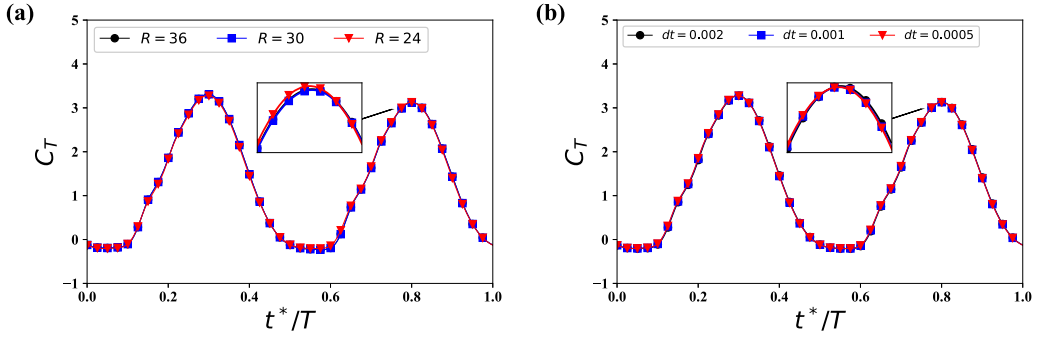

FIG. 4. (a) the effects of the radius R of the computational domain and (b) the effects of the simulation time-step (dt) for the two-dimensional flapping airfoil with kinematic parameters ($f = 0.25$, $h = 1$, $\theta_0 = 30^\circ$).

spanwise mesh size $dz = 0.02c$ and aspect ratio $AR = 1$ is chosen for the following 3D effect investigations.

For the 3D effect, in the current work, we ignore the extrinsic 3D instability triggered by wing-tip effect and only concern the intrinsic 3D instability. Three specific cases are selected: (a) $f = 0.25$, $h = 1$, $\theta_0 = 30^\circ$; (b) $f = 0.3$, $h = 1$, $\theta_0 = 5^\circ$; (c) $f = 0.4$, $h = 1$, $\theta_0 = 5^\circ$. The corresponding isosurfaces of the streamwise vorticity field are shown in Fig. 6. When the frequency is $f = 0.3$, which corresponds to asymmetry wake, 3D instability emerges. When the frequency is $f = 0.4$, 3D effects become more remarkable. By further examining the corresponding thrust coefficients, it is found that 3D instability affects the thrust coefficient results, but the trend of thrust coefficient is still consistent between 2D and 3D simulations, as shown in Fig. 7. In the meanwhile, the range of flapping frequency in the current study is $0.06 \leqslant f \leqslant 0.3$. The case with strong 3D instability ($f = 0.4$) is beyond this range. Therefore, we can assume that the 3D effect can be ignored in the present work.

E. Combination of DMD and virtual force calculation

In the post processing, the wake fields are analyzed by the DMD method, which is a dimensionality reduction algorithm developed to reduce the dimensionality of a given time-series data set, see the details in Appendix B. By using DMD, the velocity fields can be decomposed into

$$\mathbf{U}(x, t_i) = \sum_{j=0}^{n} \alpha_j \lambda_j^{i-1} \Phi_j(x), \tag{10}$$

where t_i means the ith snapshot, α_j is the modulus of jth mode, λ_j is the corresponding jth eigenvalue, and Φ_j is the jth DMD mode of the velocity field. Since the complex eigenvalues are conjugated, the corresponding DMD modes are also conjugated and we have added up the conjugated DMD mode pairs in the following calculations:

$$\mathbf{U}'(x, t_i) = \sum_{j=0}^{m/2} \left(\alpha_j \lambda_j^{i-1} \Phi_j + \overline{\alpha_j} \overline{\lambda_j}^{i-1} \overline{\Phi_j}\right) = \sum_{j=0}^{m/2} a_{ij} \mathbf{U}_j, \tag{11}$$

where $\mathbf{U}'(x, t_i)$ is the reconstructed velocity field only using the conjugated DMD modes, m is the number of these conjugate modes and it is even. $\mathbf{U}_j$ is the new jth DMD mode obtained by summing two conjugated modes to eliminate the imaginary part, and a_{ij} is the new coefficient corresponding to the ith snapshot and jth DMD mode.

Furthermore, to investigate the relationship between the DMD modes and aerodynamic forces, the virtual force calculation is applied on these DMD modes. It can evaluate the fluid dynamic forces on immersed bodies by only using the velocity field [26]. Mainly three kinds of formulas can be used: "momentum equation," "impulse equation," and "flux equation." In the current work, the "momentum equation"

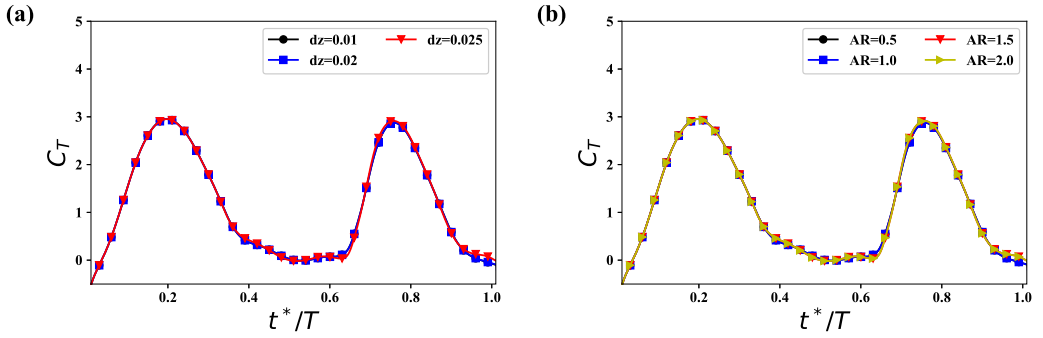

FIG. 5. The mesh validation for 3D flapping airfoil with the kinematic parameters ($f = 0.3, h = 1, \theta_0 = 5^\circ$): (a) the effects of the spanwise mesh size with fixed aspect ratio ($AR = 1$); (b) the effects of the aspect ratio with fixed spanwise mesh size ($dz = 0.02c$).

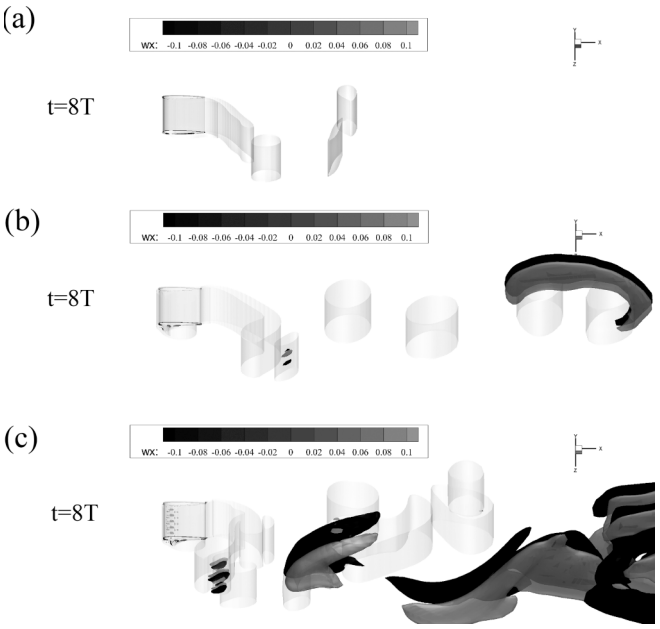

FIG. 6. The instantaneous streamwise vorticity field of three specific cases at $t = 8$ T: (a) $f = 0.25$, $h = 1$, $\theta_0 = 30°$, St $= 0.5$ (RBvK wake); (b) $f = 0.3$, $h = 1$, $\theta_0 = 5°$, St $= 0.6$ (asymmetric wake); (c) $f = 0.4$, $h = 1$, $\theta_0 = 5°$, St $= 0.8$ (beyond the parameter range in the current study). The isosurfaces are drawn transparent on the level of the spanwise vorticity equals ± 2, and the isosurfaces of streamwise vorticity with values of ± 0.1 are further drawn to evaluate the intensity of 3D instability.

is adopted due to its easy implementation and accuracy in prediction. It is defined as

$$\mathbf{F} = -\frac{d}{dt}\int_{S(t)} \mathbf{U} dS - \oint_{l(t)} \mathbf{n}\cdot\boldsymbol{\gamma}_{\mathrm{mom}} dl - \oint_{l_b(t)} \mathbf{n}\cdot(\mathbf{U}-\mathbf{u}_l)\mathbf{U} dl, \tag{12}$$

where $S(t)$ is the control volume, it is fixed, and it must contain the immersed body. $l(t)$ is the outer boundary of the control volume, $\mathbf{U}$ is the velocity of the fluid, $l_b(t)$ is the boundary of the immersed body, $\mathbf{n}$ is the outward unit normal vector of corresponding boundary, and $\mathbf{u}_l$ is the velocity of corresponding boundary. Since the boundary condition of the airfoil is no-slip/penetration, $\mathbf{n}\cdot(\mathbf{U}-\mathbf{u}_l)|_b = 0$. And $\boldsymbol{\gamma}_{\mathrm{mom}}$ is defined as

$$\boldsymbol{\gamma}_{\mathrm{mom}} = \tfrac{1}{2}|\mathbf{U}|^2\mathbf{I} - \mathbf{U}(\mathbf{U}-\mathbf{u}_l) - \mathbf{U}(\mathbf{x}\times\boldsymbol{\omega}) + \boldsymbol{\omega}(\mathbf{x}\times\mathbf{U}) - \left(\mathbf{x}\cdot\frac{\partial\mathbf{U}}{\partial t}\right)\mathbf{I} + \mathbf{x}\frac{\partial\mathbf{U}}{\partial t} + \mathbf{T} + \mathbf{x}\cdot(\nabla\cdot\mathbf{T})\mathbf{I} - \mathbf{x}(\nabla\cdot\mathbf{T}), \tag{13}$$

with

$$\mathbf{T} = \mu(\nabla\mathbf{U} + \nabla\mathbf{U}^T), \tag{14}$$

$$\boldsymbol{\omega} = \nabla\times\mathbf{U}. \tag{15}$$

Furthermore, after the spatial and temporal discretizations using central difference, the force calculation results can be

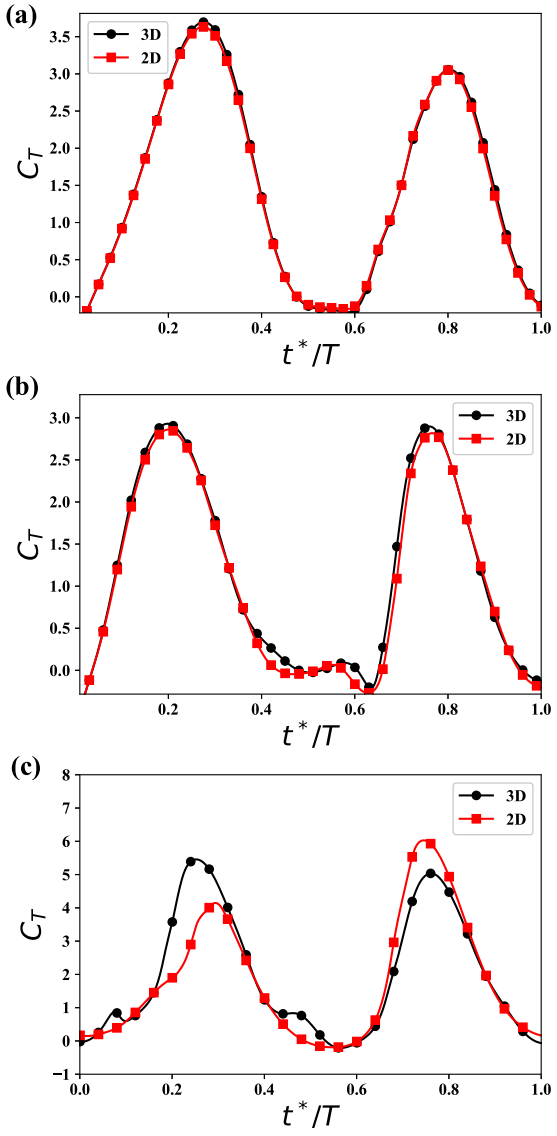

FIG. 7. The comparison between the 2D and 3D thrust coefficient results: (a) $f = 0.25$, $h = 1$, $\theta_0 = 30°$ (RBvK wake); (b) $f = 0.3$, $h = 1$, $\theta_0 = 5°$ (asymmetric wake); (c) $f = 0.4$, $h = 1$, $\theta_0 = 5°$ (beyond the parameter range in the current study).

divided into two parts, one component caused by every single mode:

$$\mathbf{F}_i^k = -\sum_m \mathbf{n}_m\cdot\boldsymbol{\gamma}_{\mathrm{mom}kim}\Delta l_m - \frac{\sum_m a_{(k+1)i}\mathbf{U}_{im}\Delta S_m - \sum_m a_{(k-1)i}\mathbf{U}_{im}\Delta S_m}{2\Delta t}, \tag{16}$$

with

$$\boldsymbol{\gamma}_{\mathrm{mom}ki} = \tfrac{1}{2}a_{ki}^2|\mathbf{U}_i|^2\mathbf{I} - a_{ki}^2\mathbf{U}_i\mathbf{U}_i - a_{ki}\mathbf{U}_i(\mathbf{x}\times a_{ki}\boldsymbol{\omega}_i) + a_{ki}\boldsymbol{\omega}_i(\mathbf{x}\times a_{ki}\mathbf{U}_i) + \mathbf{T}_i + \mathbf{x}\cdot(\nabla\cdot\mathbf{T}_i)\mathbf{I} - \mathbf{x}(\nabla\cdot\mathbf{T}_i) + \mathbf{x}\frac{a_{(k+1)i}\mathbf{U}_i - a_{(k-1)i}\mathbf{U}_i}{2\Delta t} - \left(\mathbf{x}\cdot\frac{a_{(k+1)i}\mathbf{U}_i - a_{(k-1)i}\mathbf{U}_i}{2\Delta t}\right)\mathbf{I} \tag{17}$$

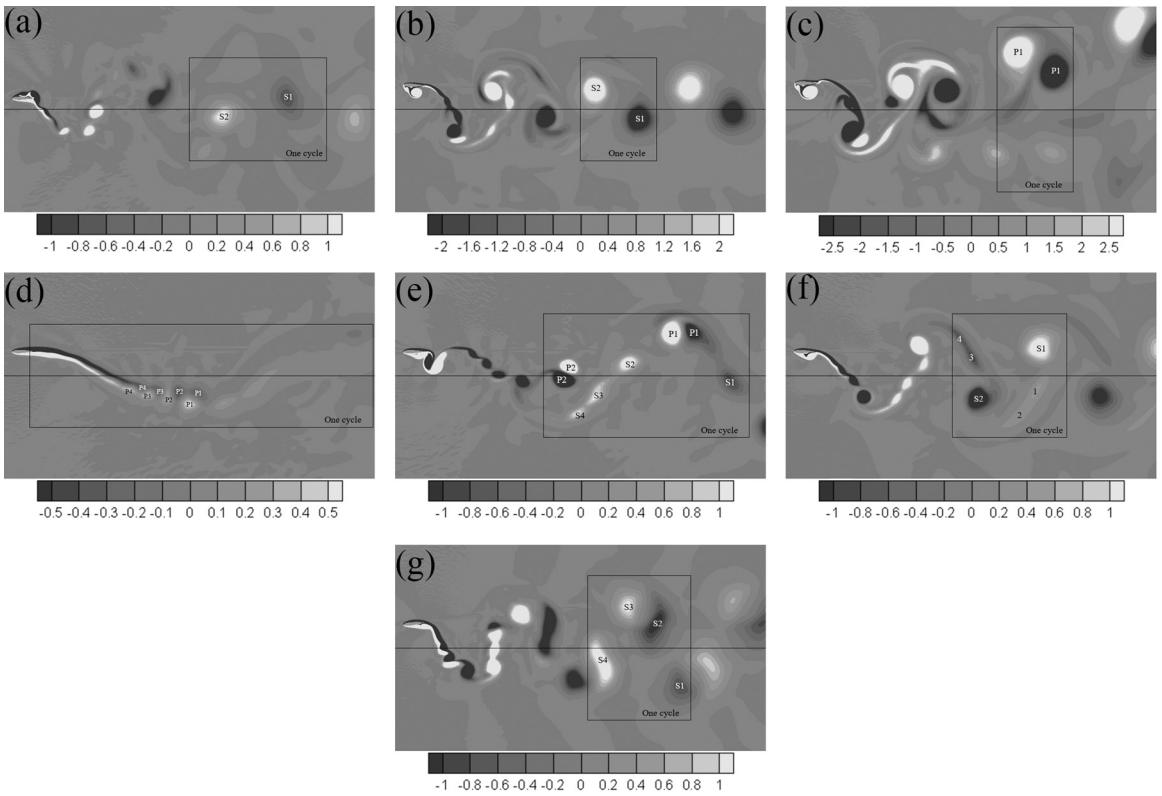

FIG. 8. The vorticity contours of the seven types of wakes: (a) the BvK wake ($f = 0.15, h = 0.375, \theta = 50^\circ$); (b) the RBvK wake ($f = 0.275, h = 1, \theta = 20^\circ$); (c) the asymmetric wake ($f = 0.30, h = 1, \theta = 5^\circ$); (d) the mP wake ($f = 0.06, h = 1, \theta = 30^\circ$); (e) the $2P + mS$ wake ($f = 0.10, h = 1, \theta = 5^\circ$); (f) the $2S + mS$ wake ($f = 0.18, h = 1, \theta = 30^\circ$); (g) the mS wake ($f = 0.20, h = 1, \theta = 50^\circ$). The middle line is the equilibrium position of the heaving motion and the box contains the wake of one period.

and another component caused by the interactions between any two modes:

$$\mathbf{F}_{ij}^{k} = \sum_{m} \mathbf{n}_m \cdot \left[\frac{1}{2} a_{ki} a_{kj} |\mathbf{U}_{im}\mathbf{U}_{jm}| - a_{ki}a_{kj}\mathbf{U}_{im}\mathbf{U}_{jm} - a_{ki}\mathbf{U}_{jm}(\mathbf{x}_m \times a_{kj}\mathbf{U}_{jm}) + a_{ki}\mathbf{U}_{im}(\mathbf{x}_m \times a_{kj}\mathbf{U}_{jm}) \right] \Delta l_m, \tag{18}$$

where Δt is the sample interval of snapshots, and the subscript m denotes the corresponding physical quantities of the mth line or surface element, the subscript k denotes the corresponding physical quantities of the kth snapshot.

III. WAKE MAP

In this section, we will reveal the correlation between the wake structures and the aerodynamic performance of the flapping airfoil.

Based on the simulation cases, the observed wake flows can be labeled into seven categories by using the symbols introduced by William and Roshko [27], where $xS + yP$ signifies x single vortices and y vortex pairs shedding per oscillation period. Figure 8 shows: (a) a $2S$ wake that evolves downstream to a BvK, (b) a inverted $2S$ wake that evolves downstream to a RBvK, (c) a $1P$ wake that is asymmetric, (d) a mP wake with multiple vortex pairs, (e) a $2P + mS$ wake consists of two dominated vortex pairs and multiple weak single vortices, (f) a $2S + mS$ wake consists of two dominated single vortices and multiple weak single vortices, (g) a mS wake with multiple single vortices.

Two phase diagrams are constructed for the wake types in terms of the flapping frequency, heaving and pitching amplitudes, as shown in Fig. 9. In the meanwhile, the parameter space can be divided into three regions: the natural shedding region including the mP wake, the harmonic region including the $2P + mS$, $2S + mS$, and mS wakes and the vortex lock-in region including the $2S$ (BvK, RBvK) and $1P$ wakes [28,29].

In group 1, at the low pitching amplitude regime ($\theta_0 \leqslant 0.35$), with the increase of flapping frequency, the flow wake transforms from the mP to $2P + mS$, then to $2S + mS$, further to RBvK, and eventually to the $1P$ wake. In group 2, a similar behavior emerges in the phase diagram with the increase of heaving amplitude. Importantly, the RBvK occurs in the regime with low pitching amplitude and high flapping frequency or heaving amplitude. At the high pitching amplitude regime, the transition between every two types of the wakes is delayed to a higher flapping frequency and heaving amplitude, which is coincident with the previous study [30]. More importantly, we have combined the isolines of propulsive efficiency with the phase diagrams. As Fig. 9 shows, the boundaries between every two types of wakes almost coincide with the isolines. Some types of wakes, such as the BvK, the mP, $2P + mS$ and mS wakes, are located at the low-efficiency regime. The best propulsive performance occurs in

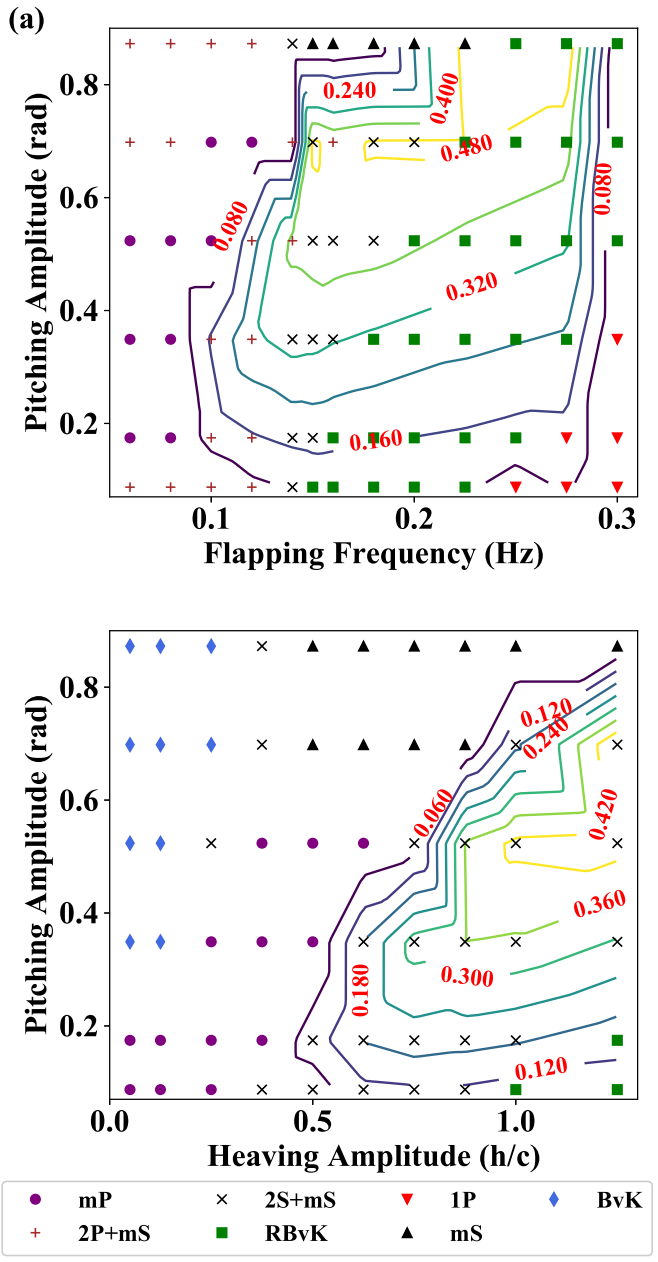

FIG. 9. The wake maps and propulsion efficiency isolines: (a) Group 1; (b) Group 2.

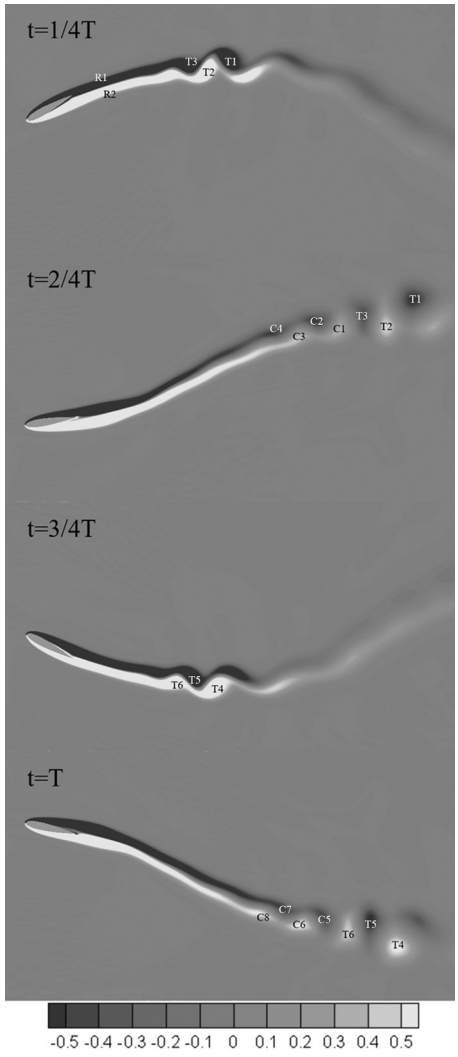

FIG. 10. The development of vortices in mP ($f = 0.06, h = 1, \theta = 30^\circ$) wake in one period.

the RBvK wake and increasing the pitching amplitude is an effective way of improving efficiency. Specifically, the vortex dynamics analyses for the four nontraditional types of wakes are carried out. For the mP wake, a row of vortex pairs is intermittently generated. As Fig. 10 shows, since the AOA is quite small, the vortex rows ("R1," "R2") with almost equal strength shed from the airfoil. In the meanwhile, by the end of an up- or down-stroke, the sign of the AOA changes, which causes a perturbation in the wake, leading to the generation of multiple vortex pairs. Compared with the natural shedding phenomenon [28,29], these vortex pairs have different morphological characteristics, such as "cats eyes" ("C1–C8") and "teardrop-shaped" ("T1–T6") structures in Fig. 10. They are elongated along the parallel and perpendicular directions of the vortex rows "R1" and "R2," respectively. Besides, there is no vortex shedding for a fixed NACA0015 airfoil at Re = 1100, which is different from the definition of natural shedding phenomenon.

For the $2P + mS$ wake in Fig. 11, since the AOA is larger than that of the mP wake, several weak trailing-edge vortices emerge, and they develop into a dominated vortex pairs $2P$ ("P1," "P2") by the end of an up- or down-stroke. Moreover, the two vortex rows become more unstable than those of mP wake, causing one of the vortex rows dissipating and mS ("S1–S8") appearing in the downstream.

By increasing the flapping frequency, the dominated vortex pairs $2P$ will change into $2S$ ("S1," "S2") structures due to its interaction with the mS vortices, leading to the occurrence of the $2S + mS$ wake, as Fig. 12 shows. By the further combination of the mS and $2S$, a $2S$ (RBvK, "S1," "S2") wake eventually emerges by further increasing the flapping frequency as shown in Fig. 13.

From the aspect of vortex structure, the $2S + mS$ and $2S$ wakes are indeed very similar. But there are some differences between them in the far wake, depending on the intensity of

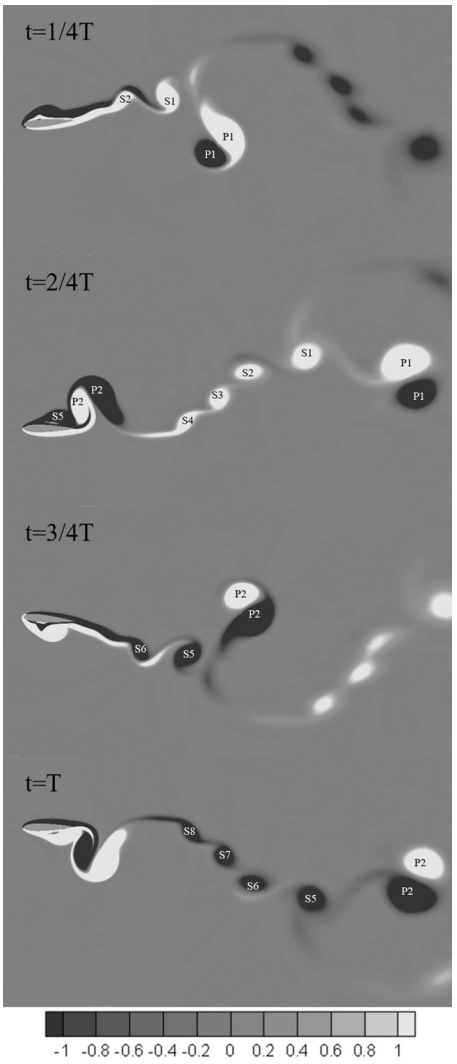

FIG. 11. The development of vortices in $2P + mS$ ($f = 0.10, h = 1, \theta = 5°$) wake in one period.

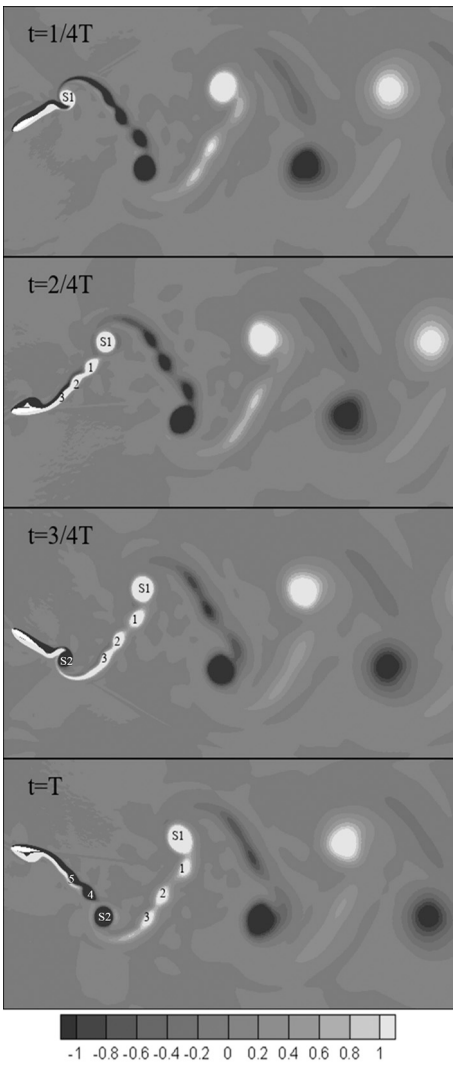

FIG. 12. The development of vortices in $2S + mS$ ($f = 0.18, h = 1, \theta = 30°$) wake in one period.

the small vortices. For the RBvK wake, the vortex shedding frequency of the dominated vortices is equal to the flapping frequency, thus the wake belongs to the lock-in region. For the $2S + mS$ wake, since the strength of mS is comparable with that of the dominated vortex $2S$, the vortex shedding frequency should be a combination of mS and $2S$, thus the wake belongs to the harmonic region.

However, by increasing the pitching amplitude at a moderate heaving amplitude or flapping frequency, although there is no obvious LEV when $\theta_0 > 0.8$, the instability and strength differences of the vortex pairs are strong, causing its transformation into single vortices, resembling the mS ("S1–S7") wake, as shown in Fig. 14.

IV. THE IMPACT OF ANGLE OF ATTACK

In this section, we will introduce another significant parameter: effective AOA, to further study the vortex dynamics of the near-wake flow field. It is defined as

$$\alpha(t) = \theta(t) - \arctan\left(\frac{\dot{y}(t)}{U_\infty}\right) \tag{19}$$

Since the calculated AOA is sinusoidal-like in one flapping period, the value at $t = T/4$ can indicate not only the changing rule of AOA but also the maximum or minimum AOA. As Fig. 15 shows, the isolines of $\alpha(\frac{T}{4})$ are combined with the corresponding wake maps. It is found that these isolines coincide with the boundaries of various wake types. The negative $\alpha(\frac{T}{4})$ is corresponding to drag-dominated flow wakes, such as BvK. While the positive $\alpha(\frac{T}{4})$ is corresponding to the thrust-dominated wakes, such as the RBvK and $1P$ wake. When the magnitude is small, $|\alpha(\frac{T}{4})| \leqslant 0.2$, the mP and mS wakes are the dominant flow regime. Moreover, the magnitude of $\alpha(\frac{T}{4})$ increases with the increase of the flapping frequency or heaving amplitude, and an opposite behavior appears with the increase of the pitching amplitude.

Specifically, seven typical cases are analyzed in Fig. 16 by investigating the effects of the AOA on the flow wake transitions and propulsion performances. In every snapshot, there is a sketch of AOA on the pivot point of the flapping airfoil, where U_x is the free-stream velocity, U_y is the relative velocity due to the airfoil's movement in the y direction, the angle

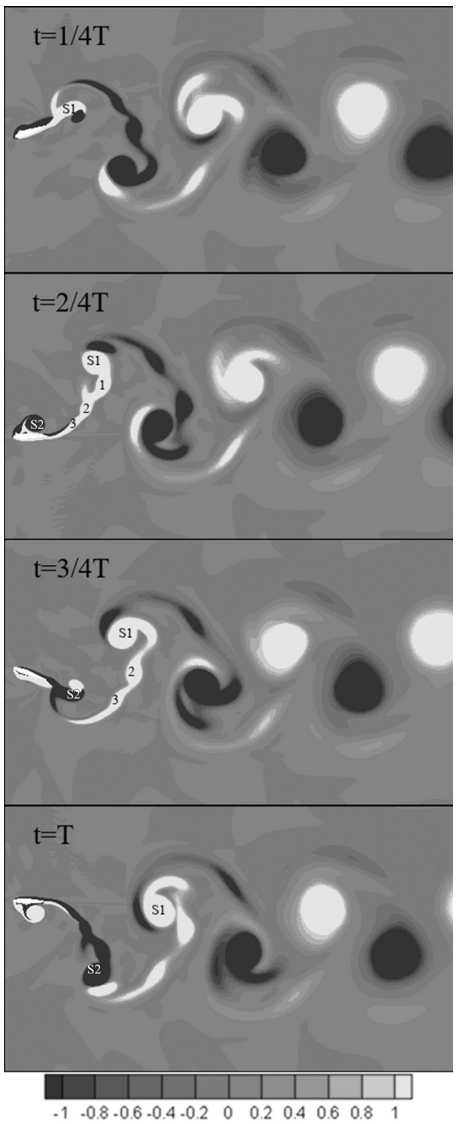

FIG. 13. The development of vortices in $2S$ (RBvK, $f = 0.275, h = 1, \theta = 20^\circ$) wake in one period.

from the airfoil chord to the resultant velocity is the AOA. As Figs. 16(a) and 16(b) show, by increasing the flapping frequency, $\alpha(\frac{T}{4})$ changes from negative value to the positive value. When $|\alpha(\frac{T}{4})| \leqslant 0.2$, there is no LEV, even though the vorticity is attached to the surface of the foil. Its intensity can determine the magnitude of $\alpha(\frac{T}{4})$, leading to the transition of

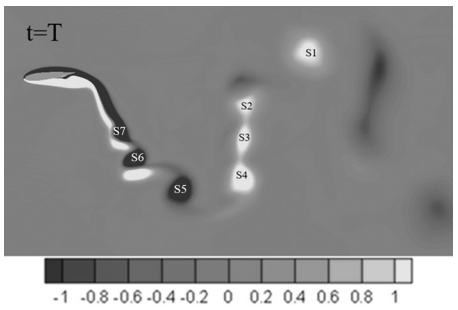

FIG. 14. The mS ($f = 0.18, h = 1, \theta = 50^\circ$) wake.

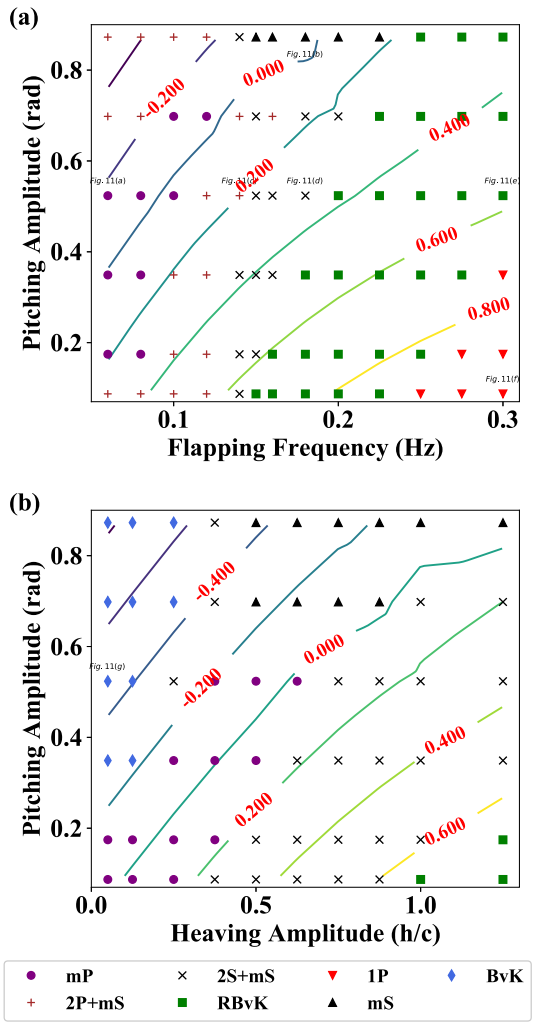

FIG. 15. The wake maps and isolines of $\alpha(\frac{T}{4})$: (a) Group 1, (b) Group 2.

wake from mP to $2P + mS$. When $\alpha(\frac{T}{4})$ is further increased, the LEVs start to separate from the upper surface and shed into the near wake, as can be seen in Figs. 16(c)–16(e). In the meanwhile, the strengths of the dominated single vortices and vortex pairs are enhanced, causing the wake transition from $2P + mS$ to $2S + mS$ to $2S$ (RBvK). When $\alpha(\frac{T}{4}) > 0.6$, all the $2S + mS$ wakes have completely transformed into the RBvK ($2S$) wake. While when the $\alpha(\frac{T}{4})$ is further increased to 0.8, the symmetry-breaking phenomenon begins to appear and the RBvK turns into the $1P$ wake.

Moreover, the correlation between the $\alpha(\frac{T}{4})$ and aerodynamic forces is analyzed. For the BvK wake, the $\alpha(\frac{T}{4})$ is negative, the drag is dominated. As for the mP, mS, and $2P + mS$ wakes, both the lift and thrust are small since no LEV is generated. As for the $2S + mS$, RBvK ($2S$), and $1P$ wakes, since $\alpha(\frac{T}{4})$ is gradually increased, the LEVs are very active in these wakes. The corresponding time-varying lift and thrust coefficients and the pressure contours at $t = T/4$ and $t = 3T/4$ are shown in Fig. 17. The arrow denotes the direction of the pressure force component, pointing to the low-pressure area. It is seen that due to the LEVs, the pressure on the upper surface of the flapping airfoil is lower at $t = T/4$.

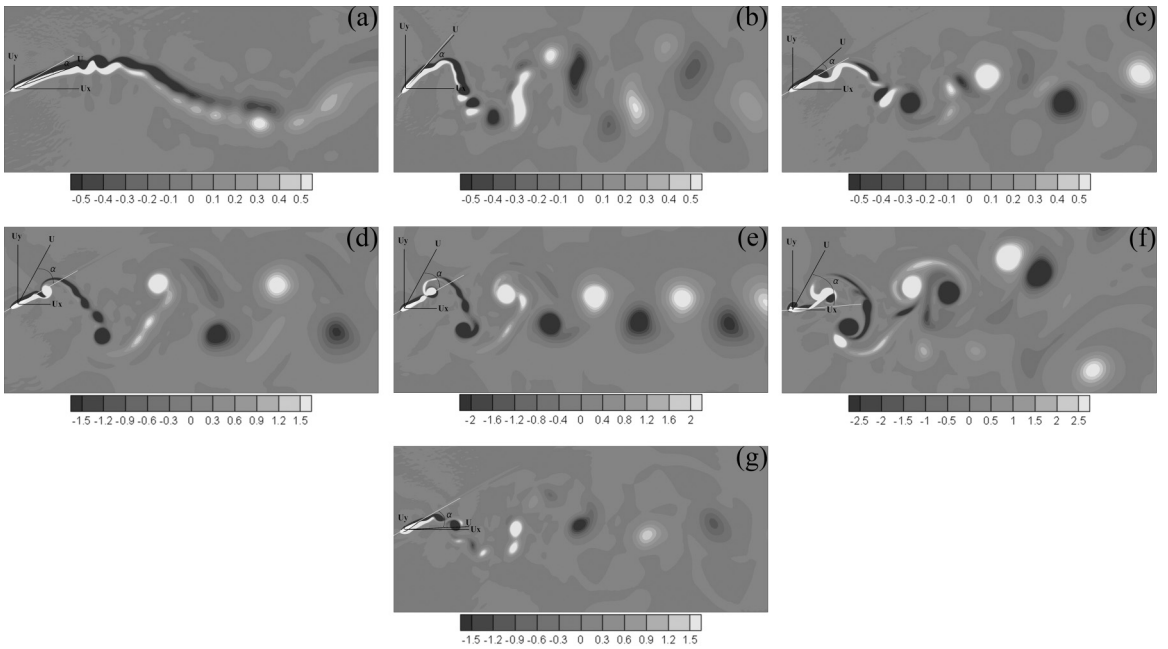

FIG. 16. The vorticity contour of seven types of wakes at $t = T/4$. (a) The mP wake [$f = 0.6,\ h = 1,\ \theta_0 = 30^\circ, \alpha(\frac{T}{4}) = -0.163$], $\overline{C_T} = -0.11$, Max(C_L) = 0.23; (b) the mS wake [$f = 0.18,\ h = 1,\ \theta_0 = 50^\circ, \alpha(\frac{T}{4}) = -0.026$], $\overline{C_T} = -0.08$, Max(C_L) = 0.57; (c) the $2P + mS$ wake [$f = 0.14, h = 1, \theta_0 = 30^\circ, \alpha(\frac{T}{4}) = 0.198$], $\overline{C_T} = 0.13$, Max(C_L) = 0.65; (d) the $2S + mS$ wake [$f = 0.18, h = 1, \theta_0 = 30^\circ, \alpha(\frac{T}{4}) = 0.323$], $\overline{C_T} = 0.26$, Max(C_L) = 1.24; (e) the RBvK wake [$f = 0.30, h = 1, \theta_0 = 30^\circ, \alpha(\frac{T}{4}) = 0.559$], $\overline{C_T} = 1.91$, Max(C_L) = 7.88; (f) the $1P$ wake [$f = 0.30, h = 1, \theta_0 = 5^\circ, \alpha(\frac{T}{4}) = 0.996$], $\overline{C_T} = 0.95$, Max(C_L) = 14.49; (g) the BvK wake [$f = 0.15, h = 0.05, \theta_0 = 30^\circ, \alpha(\frac{T}{4}) = -0.476$], $\overline{C_T} = -0.46$, Max(C_L) = 1.66.

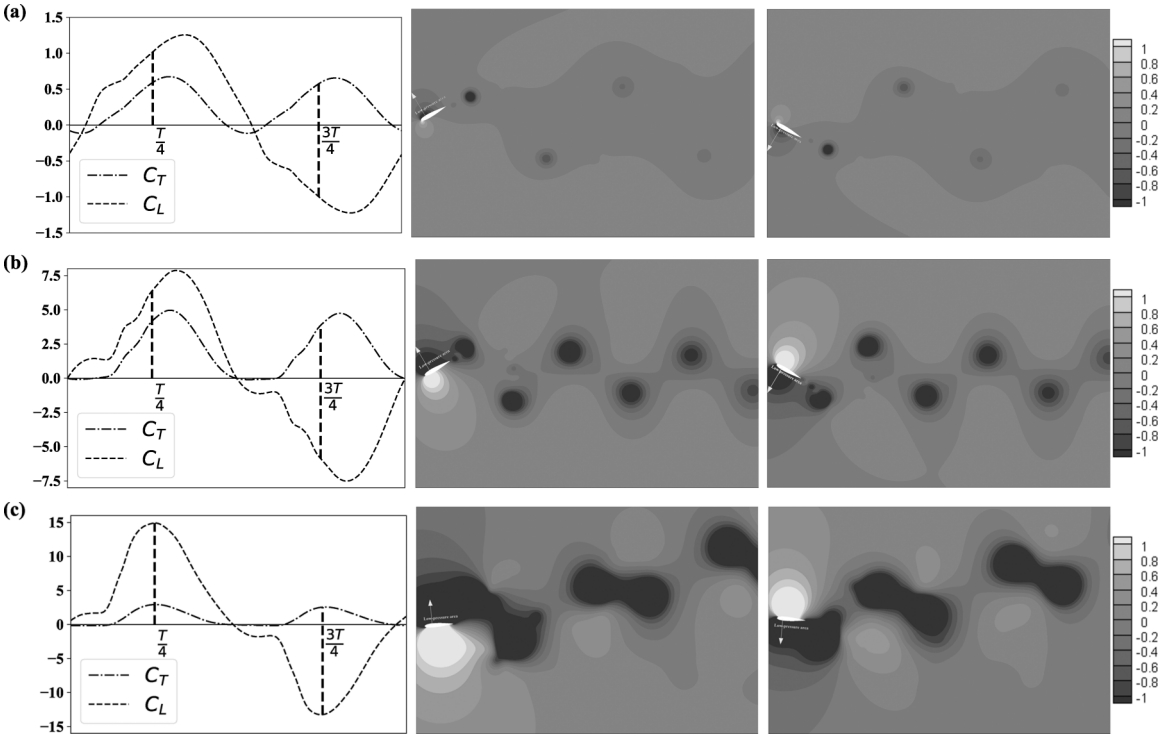

FIG. 17. The correlation between the pressure distribution and aerodynamic forces: (a) the $2S + mS$ wake [$f = 0.18,\ h = 1,\ \theta_0 = 30^\circ, \alpha(\frac{T}{4}) = 0.323$], $\overline{C_T} = 0.26$, Max(C_L) = 1.24; (b) the RBvK wake [$f = 0.30,\ h = 1,\ \theta_0 = 30^\circ, \alpha(\frac{T}{4}) = 0.559$], $\overline{C_T} = 1.91$, Max(C_L) = 7.88; (c) the $1P$ wake [$f = 0.30,\ h = 1,\ \theta_0 = 5^\circ, \alpha(\frac{T}{4}) = 0.996$], $\overline{C_T} = 0.95$, Max(C_L) = 14.49. The left column is the time-vary lift and thrust coefficients in one period, the middle column is the pressure contour at $t = T/4$, and the right column is the pressure contour at $t = 3T/4$.

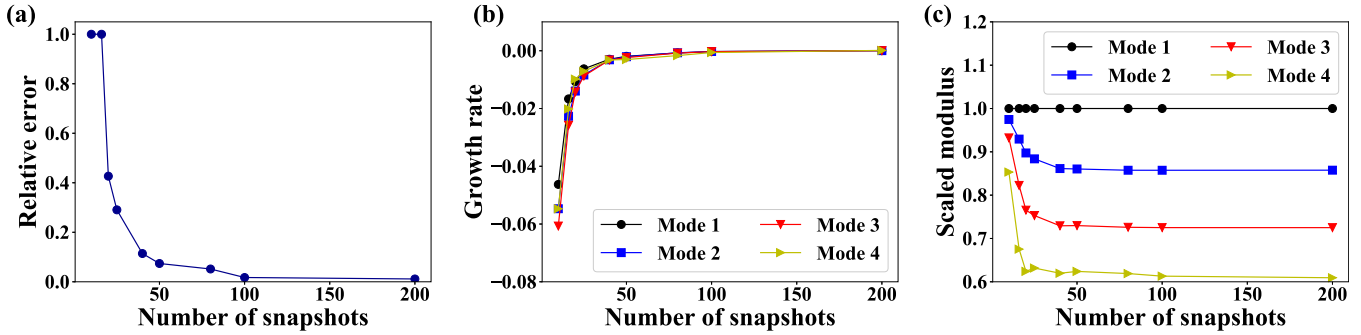

FIG. 18. The validation of the DMD analysis: (a) relative error; (b) growth rate; (c) mode modulus.

With the increase of $\alpha(\frac{T}{4})$, the low-pressure region becomes more remarkable, leading to a higher lift force coefficient. But for the transition from RBvK to $1P$ wake, the thrust force decreases since the pitching amplitude is reduced and it leads to a smaller force component in the horizontal direction.

V. MODE REDUCTION METHODS

In the previous sections, we systematically presented the wake map in various parameter spaces, and further correlated the aerodynamic performance of the flapping airfoil to the transitions among various types of wakes by introducing the important parameter: $\alpha(\frac{T}{4})$. In the following, we will apply the DMD to all the typical wake types and investigate the corresponding coherent structures and dynamic information in a quantitative way.

A. Dynamic mode decomposition

First, the convergence of the DMD analysis is validated. The relative error is defined as follows:

$$\varepsilon = \frac{||\mathbf{U}_{\text{reconst}} - \mathbf{U}||_F}{||\mathbf{U}||_F} \tag{20}$$

where $\mathbf{U}$ and $\mathbf{U}_{\text{reconst}}$ are two $m \times n$ matrices where m is the grid number of the analyzed flow field and n is the number of snapshots. $\mathbf{U}$ contains the flow field information of the simulation results, $\mathbf{U}_{\text{reconst}}$ contains the information of the reconstructed flow field and the field is reconstructed by $n-2$ DMD modes, the subscript F indicates the calculation of the Frobenius norm. The growth rate and scaled modulus are obtained by the DMD analysis and they can indicate the modes' stability and strength, respectively. As Fig. 18 shows, when the number of snapshots is beyond 100, the convergence of the performed DMD on the RBvK is reached, and similar conclusions are obtained for other types of wakes. Hence we will conduct the DMD analysis with 100 snapshots.

For all types of wakes, the first four modes (0–3) ranked by the frequency have been extracted, where the mode 0 presents the mean flow. As can be seen in the Table III, the frequency of the ith mode is approximately i times the flapping frequency.

In term of the coherent structures, it is found in Fig. 19 that all the even modes are antisymmetric while the odd modes are symmetric. Meanwhile, the specific structural characteristics of the DMD modes of the seven types of wakes are investigated here.

For the BvK wake, the mean mode indicates that there are mainly two vortex rows in the wake and the vortices in the top row rotate clockwise while in the bottom row rotate counterclockwise, as Fig. 19(a) shows; for the RBvK wake, the rotating direction of the two vortex rows in the mean mode is opposite with that of BvK, and in the mode 1, two staggered vortex rows are symmetrically distributed, as Fig. 19(b) shows; for the $1P$ wake, all the DMD modes are asymmetric, as Fig. 19(c) shows; for the mP wake, obvious vortex pairs can be observed in the modes 1–3, as shown in Fig. 19(d). For the $2P+mS$ wake, in all the DMD modes, two vortex rows get close to each other at first and then split up in the downstream, as Fig. 19(e) shows; for the $2S+mS$ wake, the vorticity fields of these DMD modes resemble those of the RBvK wake, while the difference lies in that there are two weak vortex rows between the two dominated vortex rows, which is caused by the mS, as Fig. 19(f) shows; for the mS wake, the two vortex rows in the middle becomes stronger comparing with the $2S+mS$ wake, thus four staggered vortex rows emerge in the mode 1, as Fig. 19(g) shows.

In terms of the dynamic information, the modulus and eigenvalues of all DMD modes are presented in Fig. 20. Here the modulus indicates the strength of the corresponding mode and the eigenvalue indicates the frequency and stability of the corresponding mode. Besides, the modulus of DMD modes is correlated to the vortex shedding patterns in the flow wake, i.e., the strengths of vortices shedding at i times flapping frequency are closely correlated with the modulus of the ith DMD mode.

For the mP wake, as Fig. 20(c) shows, the modulus of mode 1 is the highest, and the modulus of high-frequency modes are also remarkable, since there are multiple vortex pairs shedding per oscillation period. For the $2P+mS$ wake, mode

TABLE III. The frequencies of dominant modes for the seven types of wakes.

	Parameters$[f, h, \theta_0]$	Mode 1	Mode 2	Mode 3	Mode 4
BvK	[0.15, 0.375, 50°]	0.1477	0.2954	0.4544	0.5924
RBvK	[0.275, 1, 20°]	0.2690	0.5391	0.8117	1.0815
$1P$	[0.30, 1, 5°]	0.2958	0.5934	0.8920	1.1927
mP	[0.06, 1, 30°]	0.0620	0.1239	0.1858	0.2477
$2P+mS$	[0.10, 1, 5°]	0.1053	0.2110	0.3155	0.4200
$2S+mS$	[0.18, 1, 30°]	0.1850	0.3697	0.5545	0.7392
mS	[0.20, 1, 50°]	0.2107	0.4204	0.6289	0.8377

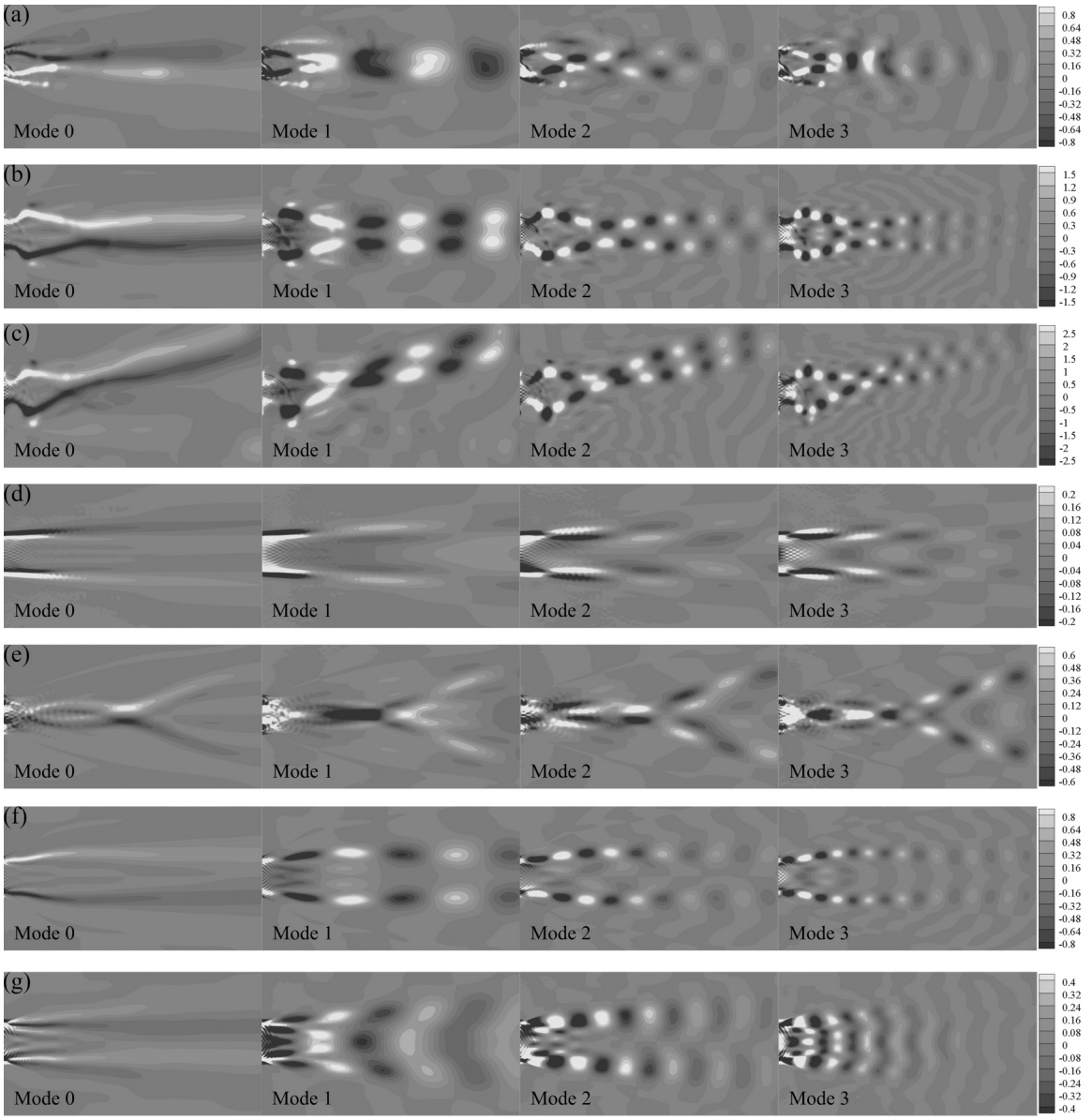

FIG. 19. The vorticity contour of the first four modes of the seven types of wakes: (a) the BvK wake ($f = 0.15,\ h = 0.375,\ \theta = 50°$); (b) the RBvK wake ($f = 0.275,\ h = 1,\ \theta = 20°$); (c) the $1P$ wake ($f = 0.30,\ h = 1,\ \theta = 5°$); (d) the mP wake ($f = 0.06,\ h = 1,\ \theta = 30°$); (e) the $2P + mS$ wake ($f = 0.10,\ h = 1,\ \theta = 5°$); (f) the $2S + mS$ wake ($f = 0.18,\ h = 1,\ \theta = 30°$); (g) the mS wake ($f = 0.20,\ h = 1,\ \theta = 50°$).

2 reaches the peak modulus because of the dominated $2P$. And since there are 3–5 single vortices in the $2P + mS$ wake, the modulus of modes 3–5 are relatively high, as Fig. 20(d) shows. For the $2S + mS$ wake, in Fig. 20(e), the modulus of mode 1 is the highest because of the dominated $2S$. And similar with the $2P + mS$ wake, the modulus of modes 2–4 are relatively high. However, as Fig. 20(a) shows, for a typical $2S$ wake, the modulus of mode 1 is the highest while the modulus of other modes are quite small, which indicates a typical lock-in region wake. For the mS wake, since the multiple single vortices partially merge and evolve downstream to a $4S$ wake, the modulus of modes 1–3 are high, as shown in Fig. 20(f). For the $1P$ wake, similar with the $2S$ wake, the dominated vortex pair shedding per period leads the highest modulus of mode 1, as shown in Fig. 20(b).

Then a new parameter ϵ is defined to quantitatively classify these wake types:

$$\epsilon = \frac{M_1 - \frac{1}{3}\sum_{i=2}^{4} M_i}{M_1}, \tag{21}$$

where M_i is the modulus of the ith mode. For the wakes in the vortex lock-in region ($1P$, $2S$), the modulus of mode 1 is the highest and $\epsilon > 18\%$. For the wakes in the harmonic region ($2P + mS$, $2S + mS$, mS), compared with the wakes in the vortex lock-in region, the value of ϵ gradually decreases and the modulus of high-frequency modes increases. And for the wake in the natural shedding region (mP) the value of ϵ is small and the modulus of high-frequency modes becomes remarkable.

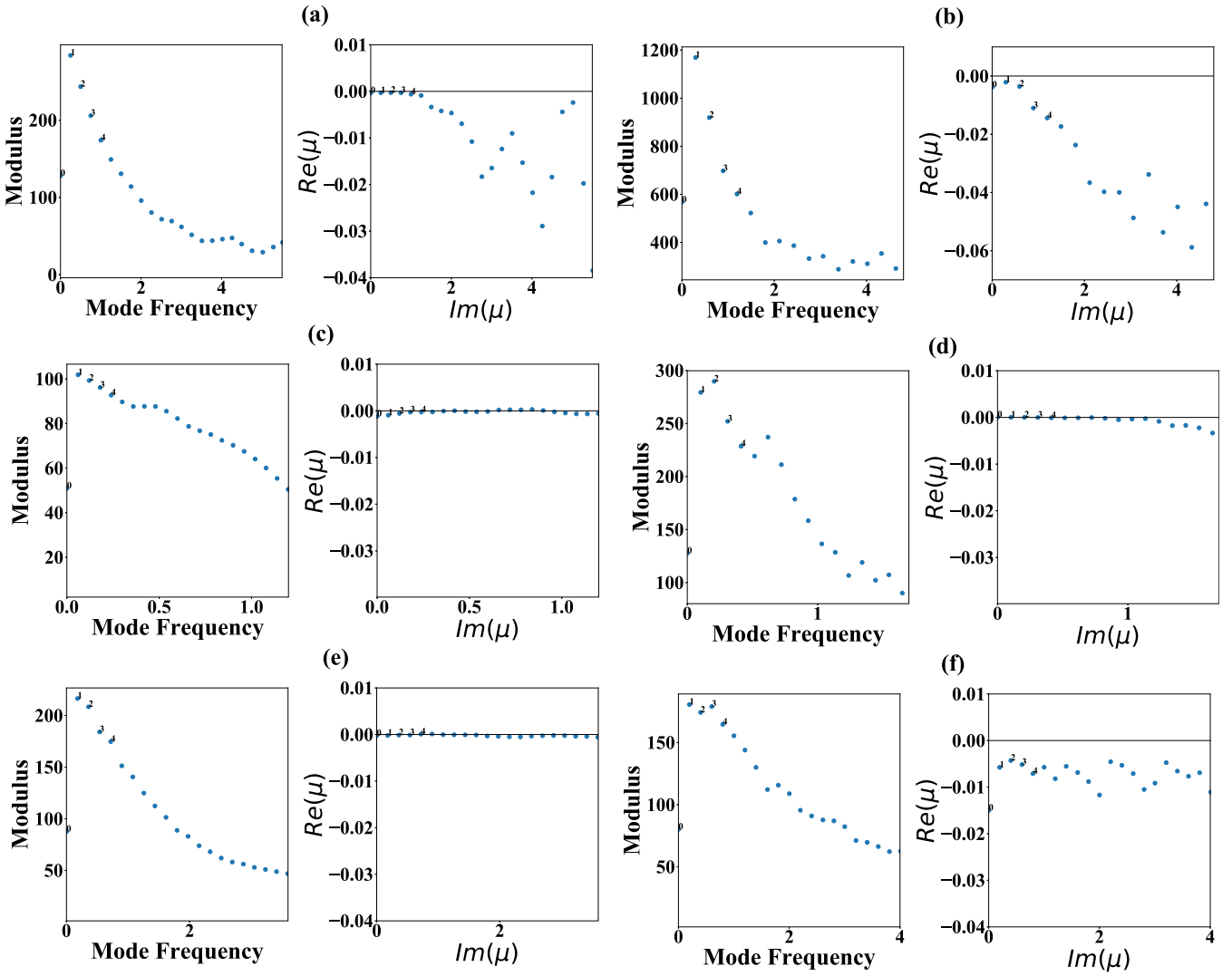

FIG. 20. The modulus and the stability analysis of the modes for the six types of wakes: (a) the RBvK wake ($f = 0.275,\ h = 1,\ \theta = 20°$), $\epsilon = 0.270$; (b) the $1P$ wake ($f = 0.30,\ h = 1,\ \theta = 5°$), $\epsilon = 0.367$; (c) the mP wake ($f = 0.06,\ h = 1,\ \theta = 30°$), $\epsilon = 0.059$; (d) the $2P + mS$ wake ($f = 0.10,\ h = 1,\ \theta = 5°$), $\epsilon = 0.079$; (e) the $2S + mS$ wake ($f = 0.18,\ h = 1,\ \theta = 30°$), $\epsilon = 0.125$; (f) the mS wake ($f = 0.20\ h = 1,\ \theta = 50°$), $\epsilon = 0.046$.

As for the stability analysis, μ is the logarithmic form of the eigenvalue λ. The real part of μ is the growth or decay rate, positive (negative) real part value denotes the unstable (stable) mode and zero value denotes the neutral stable mode. It is observed that the growth or decay rates of all the dominated DMD modes are quite small, which has no obvious physical

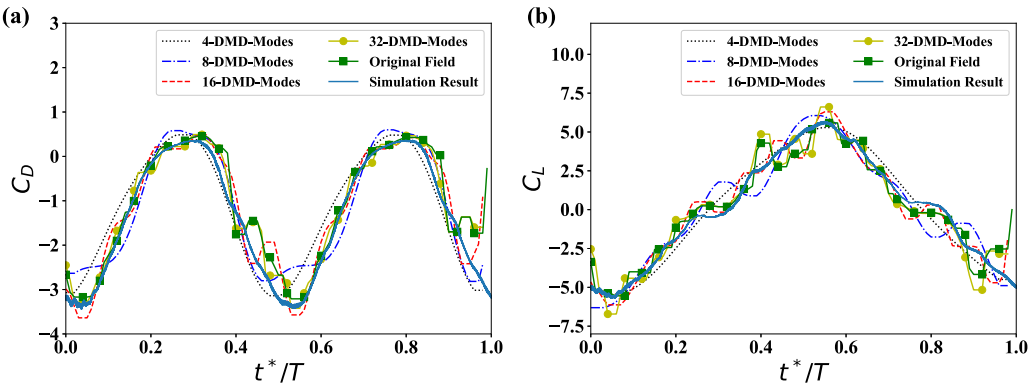

FIG. 21. The validation of the combination of DMD modes and virtual force calculation: (a) the drag coefficient, (b) the lift coefficient.

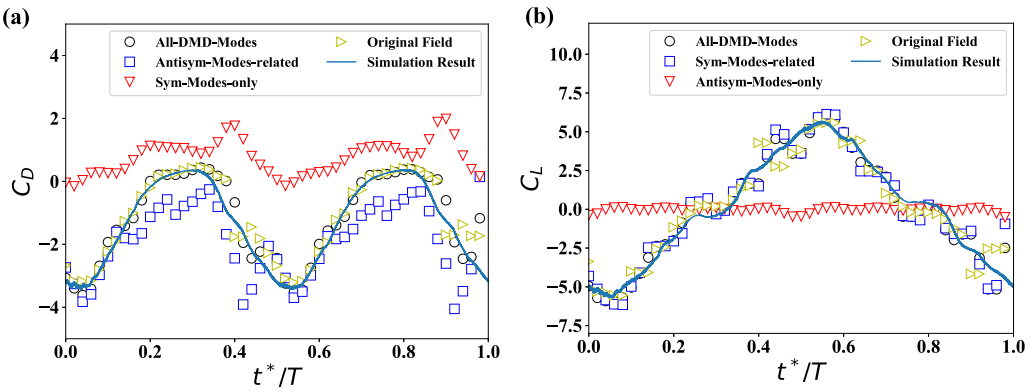

FIG. 22. The (a) drag coefficient and (b) lift coefficient of antisymmetric, symmetric, and all DMD modes in one period, which are calculated only using the velocity field.

meaning. Hence, the growth and decay of the DMD modes can be neglected, and these modes are neutral stable due to the good period property of the wakes in the current study.

B. Virtual force calculation of DMD modes

To further investigate the correlation between DMD modes and aerodynamic forces, the virtual force calculation is applied to these DMD modes. First, the virtual force calculation of DMD modes is validated against the simulation results. The flow field of a typical RBvK wake is chosen, with the kinematic parameters: $\theta_0 = 30^\circ$, $h = 1$, $f = 0.25$.

As Fig. 21 shows, the virtual force calculation of the original fields and that of reconstructed fields with a different number of DMD modes are compared against the simulation results, and a good agreement is reached. Additionally, the higher the number of the DMD modes used for the reconstruction, the better the coincidence between the virtual force calculations of the reconstructed field and the original field. In the current study, the calculation results using four modes are accurate enough. Moreover, as mentioned before, all the DMD modes can be divided into two categories: symmetric and antisymmetric. Therefore, we further divide the aerodynamic forces into four groups: $F_{\text{Sym-only}}$ ($F_{\text{Antisym-only}}$) is the sum of force components only related to symmetric (antisymmetric) modes, while $F_{\text{Antisym-related}}$ ($F_{\text{Sym-related}}$) is the sum of the rest force components by subtracting $F_{\text{Sym-only}}$ ($F_{\text{Antisym-only}}$).

By using four DMD modes, we have calculated the time-varying thrust and lift coefficients and these four components: $F_{\text{Antisym-related}}$, $F_{\text{Sym-only}}$, $F_{\text{Sym-related}}$, $F_{\text{Antisym-only}}$. As Fig. 22 shows, the thrust is produced mainly by the antisymmetric DMD modes while the lift is produced mainly by the symmetric DMD modes.

VI. CONCLUSIONS

The present study elucidates the flow mechanisms involved in the two-dimensional flapping airfoil. We correlate the aerodynamic performances with the wake structures by constructing two phase diagrams of wake types in terms of three basic parameters: frequency, heaving and pitching amplitudes, whereas only the wake map of pure heaving and pitching airfoil was presented in the previous studies. According to the number of single vortices and vortex pairs shedding per oscillating period, the wake flows are divided into seven categories. Except the well-known BvK, RBvK, and $1P$ wakes, four new types of wakes: the mP, $2P + mS$, $2S + mS$, and mS wakes are introduced. Then the effects of the important parameter $\alpha(\frac{T}{4})$ on the transitions among different types of wakes are addressed. The drag-dominated BvK wake corresponds to negative $\alpha(\frac{T}{4})$ while the thrust-dominated RBvK wake corresponds to positive $\alpha(\frac{T}{4})$. With the increase of $\alpha(\frac{T}{4})$, the wake transforms from the mP to $2S + mS$ then to RBvK and eventually to $1P$ wake.

In the post-processing, the dimensionality reduction algorithm DMD is applied to the near-wake fields of all the cases. It is found that the strengths of vortices shedding at i times flapping frequency are closely related with the modulus of the ith DMD mode. And based on the conclusion, DMD can play a subsidiary role in the wake type classification. For the wakes in the vortex lock-in region ($1P$, $2S$), the modulus of mode 1 is the highest. For the wakes in the harmonic region ($2P + mS$, $2S + mS$, mS), the modulus of mode 1 is still the highest or the second highest, but the modulus of modes 2–5 also becomes relatively high. For the wake in the natural shedding region (mP), the modulus of high-frequency modes is remarkable. And we further define the parameter ϵ to quantitatively distinguish these wakes. Moreover, we correlate the aerodynamic forces with the DMD modes. Based on the virtual force calculation results, the thrust is produced mainly by the antisymmetric DMD modes while the lift is produced mainly by the symmetric DMD modes.

ACKNOWLEDGMENT

The authors gratefully acknowledge support from the National Natural Science Foundation of China (Grant No. 11602217).

APPENDIX A: RADIAL BASIS FUNCTION INTERPOLATION

In this Appendix, we describe the theory of the radial basis function interpolation. It holds that the grid movements are only related with the motion of boundary points and the

Euclidean distances between the unsolved points and boundary points. Since the boundary points are also supposed to satisfy the interpolation equation, the interpolation coefficient can be obtained by solving an equation set, whose matrix form is as follows:

$$\begin{bmatrix} \Phi_{nn} & \mathbf{q}(\mathbf{x}_n) \\ \mathbf{q}(\mathbf{x}_n)^T & 0 \end{bmatrix} \begin{bmatrix} \boldsymbol{\alpha} \\ \boldsymbol{\beta} \end{bmatrix} = \begin{bmatrix} \mathbf{s}_n \\ 0 \end{bmatrix}, \tag{A1}$$

where Φ_{nn} is a $n \times n$ matrix, n is the number of boundary points whose displacements are known, and the elements in the matrix can be calculated by the radial basis function $\Phi_{ij} = \Phi(||\mathbf{x}_i - \mathbf{x}_j||)$, where $\mathbf{x}_i$ is the coordinates of the ith boundary point $\mathbf{x}_i = [x_i, y_i, z_i]$. $\mathbf{q}(\mathbf{x}_n)$ is a $n \times (d+1)$ matrix, d is the dimension of the mesh points, the jth row is $q(\mathbf{x}_j) = [1, \mathbf{x}_j]$, and $\mathbf{s}_n$ is the displacements of boundary points.

In the current work, we have tested the thin plate spline, inverse multiquadratic biharmonics, and Gaussian radial basis functions. It turns out that the three functions barely affect the simulation results. If the unique solution $\boldsymbol{\alpha} = [\alpha_1, \alpha_2, ..., \alpha_n]^T$, $\boldsymbol{\beta} = [\beta_0, \beta_1, ..., \beta_d]^T$ exists, the motion of arbitrary internal point $\mathbf{x}$ can be calculated:

$$s(\mathbf{x}) = \sum_{i=1}^{n} \alpha_i \Phi(||\mathbf{x} - \mathbf{x}_i||) + \beta_0 + \sum_{j=1}^{d} \beta_j \mathbf{x}[j], \tag{A2}$$

where $\mathbf{x}[j]$ is the jth element in $\mathbf{x}$. Besides, we use the absolute radial basis function interpolation with compact support. It means that only the points, whose distance from the chosen center point is less than the support radius, are influenced by the boundary points. In the meanwhile, the interpolation coefficients $\boldsymbol{\alpha}$, $\boldsymbol{\beta}$ are only calculated once at the beginning of the simulation:

$$\Phi(||\mathbf{x} - \mathbf{x}_b||) = \begin{cases} 0 & ||\mathbf{x} - \mathbf{x}_c|| > r \\ \Phi(||\mathbf{x} - \mathbf{x}_b||) & ||\mathbf{x} - \mathbf{x}_c|| \leqslant r \end{cases}, \tag{A3}$$

where $\mathbf{x}_b$ is the boundary points, $\mathbf{x}_c$ is the center point, r is the support radius.

APPENDIX B: DYNAMIC MODE DECOMPOSITION

The standard DMD algorithm we used in the present work is simply introduced here. First, the snapshots obtained by experiment or simulation can be put into a sequence, hence the data of these snapshots can form a matrix $\mathbf{V}_1^N$ as follows:

$$\mathbf{V}_1^N = [\mathbf{v}_1, \mathbf{v}_2, \mathbf{v}_3, ..., \mathbf{v}_N], \tag{B1}$$

where $\mathbf{v}_1$ is the first flow field in the sequence and $\mathbf{v}_N$ the last, and the time steps between every two snapshots are the same. A basic assumption is that there is a linear mapping $\mathbf{A}$ which maps a flow field to the field at the next moment,

$$\mathbf{v}_{j+1} = \mathbf{A}\mathbf{v}_j. \tag{B2}$$

Therefore, the matrix mentioned above can be represented as

$$\mathbf{V}_1^N = [\mathbf{v}_1, \mathbf{A}\mathbf{v}_1, \mathbf{A}^2\mathbf{v}_1, ..., \mathbf{A}^{N-1}\mathbf{v}_1], \tag{B3}$$

which is a Krylov sequence. Then a truncated singular value decomposition (TSVD) of $\mathbf{V}_1^{N-1}$ is carried out,

$$\mathbf{V}_1^{N-1} = \mathbf{U}\boldsymbol{\Sigma}\mathbf{W}^H. \tag{B4}$$

Schmid [31] presented an approximation of the matrix A,

$$\bar{\mathbf{S}} = \mathbf{U}^H\mathbf{A}\mathbf{U} = \mathbf{U}^H\mathbf{V}_2^N\mathbf{W}\boldsymbol{\Sigma}^{-1}, \tag{B5}$$

where $\bar{\mathbf{S}}$ is the similarity matrix of $\mathbf{A}$, the eigenvalue and eigenvector of $\bar{\mathbf{S}}$ are respectively λ and $\mathbf{T}$. The extracted dynamic modes Φ are as follows:

$$\Phi_j = \mathbf{U}\mathbf{T}_j. \tag{B6}$$

Since both $\mathbf{U}$ and $\mathbf{T}$ are orthogonal matrix, the dynamic modes Φ have unit norm. And the flow field can be represented as a linear combination of DMD modes:

$$\mathbf{v}_i = \sum_{j=1}^{N} \alpha_j \lambda_j^{i-1} \Phi_j, \tag{B7}$$

where α_i is the posterior amplitude of the ith mode and it can be calculated by solving the equation set whose matrix form $\mathbf{V}_1^{N-1} = \Phi \cdot \mathrm{Diag}(\alpha) \cdot \mathbf{V}_{\mathrm{and}}$:

$$[\mathbf{v}_1 \ \mathbf{v}_2 \ \cdots \ \mathbf{v}_{N-1}] = [\Phi_1 \ \Phi_2 \ \cdots \ \Phi_{N-1}] \begin{bmatrix} \alpha_1 & 0 & \cdots & 0 \\ 0 & \alpha_2 & \cdots & 0 \\ \vdots & \vdots & & \vdots \\ 0 & 0 & \cdots & \alpha_{N-1} \end{bmatrix} \begin{bmatrix} 1 & \lambda_1 & \cdots & (\lambda_1)^{N-1} \\ 1 & \lambda_2 & \cdots & (\lambda_2)^{N-1} \\ \vdots & \vdots & & \vdots \\ 1 & \lambda_{N-1} & \cdots & (\lambda_{N-1})^{N-1} \end{bmatrix}, \tag{B8}$$

where $\mathbf{V}_{\mathrm{and}}$ is the Vandermonde matrix.

For the equation set, it can be approximate to an optimization problem with the goal of finding proper α to minimize $||\mathbf{V}_1^{N-1} - \Phi\mathrm{Diag}(\alpha)\mathbf{V}_{\mathrm{and}}||$.

Furthermore, some significant information can be obtained by analyzing the Ritz values. The logarithmic form of the Ritz values provides the frequency $\mathrm{Im}[lg(\lambda)/\Delta t]$ and growth rate $\mathrm{Re}[lg(\lambda)/\Delta t]$. And Ritz values lying on the unit circle on the complex plane indicate that the corresponding modes are neutral stable with zero growth rate. While if the Ritz value lies inside or outside of the unit circle, the corresponding mode is stable and unstable, respectively [32].

[1] D. L. Ciffone and K. Orloff, J. Aircraft **12**, 464 (1975).

[2] Y. Pan, X. Dong, Q. Zhu, and D. K. Yue, J. Fluid Mech. **698**, 446 (2012).

[3] J. Deng, L. Teng, D. Pan, and X. Shao, Phys. Fluids **27**, 053103 (2015).

[4] F. M. Bos, D. Lentink, B. Van Oudheusden, and H. Bijl, J. Fluid Mech. **594**, 341 (2008).

[5] L. Sun, J. Deng, and X. Shao, Phys. Rev. E **97**, 013110 (2018).

[6] J. Deng, L. Sun, and X. Shao, Phys. Rev. E **92**, 063013 (2015).

[7] D. G. Bohl and M. M. Koochesfahani, J. Fluid Mech. **620**, 63 (2009).

[8] A. Mackowski and C. Williamson, J. Fluid Mech. **765**, 524 (2015).

[9] A. Das, R. K. Shukla, and R. N. Govardhan, J. Fluid Mech. **800**, 307 (2016).
[10] J. Young and J. C. S. Lai, AIAA J. **42**, 2042 (2004).
[11] R. Godoy-Diana, J.-L. Aider, and J. E. Wesfreid, Phys. Rev. E **77**, 016308 (2008).
[12] T. Schnipper, A. Andersen, and T. Bohr, J. Fluid Mech. **633**, 411 (2009).
[13] A. Andersen, T. Bohr, T. Schnipper, and J. H. Walther, J. Fluid Mech. **812**, R4 (2017).
[14] F. Hover, Ø. Haugsdal, and M. Triantafyllou, J. Fluids Struct. **19**, 37 (2004).
[15] L. Schouveiler, F. Hover, and M. Triantafyllou, J. Fluids Struct. **20**, 949 (2005).
[16] T. Kinsey and G. Dumas, AIAA J. **46**, 1318 (2008).
[17] S. Bagheri, J. Fluid Mech. **726**, 596 (2013).
[18] B. Podvin and Y. Fraigneau, Phys. Fluids **29**, 020709 (2017).
[19] F. Guéniat, L. Mathelin, and L. R. Pastur, Phys. Fluids **27**, 025113 (2015).
[20] A. T. Mohan, D. V. Gaitonde, and M. R. Visbal, Comput. Fluids **129**, 1 (2016).
[21] C. Pan, D. Yu, and J. Wang, Theoret. Appl. Mech. Lett. **1**, 012002 (2011).
[22] Z. Liang and H. Dong, Phys. Fluids **27**, 063601 (2015).
[23] H. G. Weller, G. Tabor, H. Jasak, and C. Fureby, Comput. Phys. **12**, 620 (1998).
[24] C. Hirt, A. Amsden, and J. Cook, J. Comput. Phys. **135**, 203 (1997).
[25] F. M. Bos, Numerical simulations of flapping foil and wing aerodynamics: Mesh deformation using radial basis functions, Ph.D. thesis, Delft University of Technology, 2010.
[26] F. Noca, D. Shiels, and D. Jeon, J. Fluids Struct. **13**, 551 (1999).
[27] C. H. Williamson and A. Roshko, J. Fluids Struct. **2**, 355 (1988).
[28] J. Young and J. C. Lai, AIAA J. **45**, 485 (2007).
[29] D. Cleaver, D. E. Calderon, Z. Wang, and I. Gursul, Exp. Fluids **54**, 1491 (2013).
[30] J. Anderson, K. Streitlien, D. Barrett, and M. Triantafyllou, J. Fluid Mech. **360**, 41 (1998).
[31] P. J. Schmid, J. Fluid Mech. **656**, 5 (2010).
[32] C. W. Rowley, I. Mezić, S. Bagheri, P. Schlatter, and D. S. Henningson, J. Fluid Mech. **641**, 115 (2009).